Synthesis and Radioluminescence of PEGylated Eu³⁺-doped Nanophosphors as Bioimaging Probes

Conroy Sun,
Molecular Imaging Program at Stanford Stanford University Stanford, CA 94305, USA

Department of Radiation Oncology School of Medicine Stanford University Stanford CA 94305, USA

Guillem Pratx,
Molecular Imaging Program at Stanford Stanford University Stanford, CA 94305, USA

Department of Radiation Oncology School of Medicine Stanford University Stanford CA 94305, USA

Colin M. Carpenter,
Molecular Imaging Program at Stanford Stanford University Stanford, CA 94305, USA

Department of Radiation Oncology School of Medicine Stanford University Stanford CA 94305, USA

Hongguang Liu,
Molecular Imaging Program at Stanford Stanford University Stanford, CA 94305, USA

Department of Radiology School of Medicine Stanford University Stanford, CA 94305, USA

Zhen Cheng,
Molecular Imaging Program at Stanford Stanford University Stanford, CA 94305, USA

Department of Radiology School of Medicine Stanford University Stanford, CA 94305, USA

Sanjiv Sam Gambhir, and
Molecular Imaging Program at Stanford Stanford University Stanford, CA 94305, USA

Department of Radiology School of Medicine Stanford University Stanford, CA 94305, USA

Lei Xing[*]
Molecular Imaging Program at Stanford Stanford University Stanford, CA 94305, USA

Department of Radiation Oncology School of Medicine Stanford University Stanford CA 94305, USA

Lanthanide-doped nanophosphors have received significant attention for use in biological sensing and imaging due to their unique optical properties. Much like semiconductor

[*]lei@stanford.edu.

quantum dots (QDs), these luminescent nanocrystals offer several advantages over conventional organic fluorophores, including high photochemical stability, large Stokes shift, and tunable fluorescence emission. [1] Up-conversion nanophosphors, which are capable of absorbing two or more low-energy photons to emit a higher-energy photon, also exhibit favorable characteristics such as long fluorescence lifetimes, no photoblinking, and reduced autofluorescence. [2] The recent development of lanthanide-doped nanophosphors that function in the near-infrared (NIR) spectral range optimal for optical transmission through biological tissues (650–900 nm) has attracted great interest towards in vivo bioimaging probes. [3–5] Alternatively, high-energy radiation, currently employed in medical imaging modalities, such as X-ray computed tomography (CT) or positron emission tomography (PET), may also be used to excite NIR-emitting radioluminescent nanophosphors (RLNPs) for bioimaging.

Recently, RLNPs have been proposed as molecular imaging probes in the development of combined X-ray/optical imaging modalities, such as X-ray luminescence computed tomography (XLCT). [6–8] This innovative imaging technique provides deep tissue penetration, circumvents tissue autofluorescence, and simplifies imaging through optical reconstruction from planar images. Tissue-specific accumulation of these RLNPs through molecular targeting strategies [9, 10] would allow for localization of lesions, such as tumors, through detection of luminescence induced by narrowly collimated X-rays. In addition, RLNPs capable of activation by radioisotopes, such as PET tracers and radiopharmaceuticals, may enable planar optical detection of radiotherapy or co-localization of molecular targets. To enable these novel imaging modalities, we present a facile procedure to synthesize poly(ethylene glycol) (PEG)-coated RLNPs and examine their ability to serve as optical probes excited by X-rays or radioisotopes.

Conventional X-ray phosphor synthesis processes (e.g., solid state or molten flux reactions) are limited in their ability to produce colloidal and monodispersed nanocrystals for biological applications. In this work, we utilize a solution-based thermal degradation of organometallic precursors to produce europium-doped barium yttrium fluoride nanophosphors with a uniform morphology and narrow size distribution (**Figure 1** A). Adapted from an up-conversion nanophosphor synthesis route reported by Capobianco et al., [11] this procedure employs a well-established octadecene/oleic acid reaction medium to control nucleation and growth of the crystals. [12,13] Here a europium trifluoracetate (TFA) precursor was used to incorporate trivalent europium (Eu^{3+}) as a luminescence activator. Oleic acid-capped RLNP produced by this procedure (Figure 1 B) are hydrophobic and quickly flocculated when transferred into water (Figure 1 C). To enable use under aqueous conditions, surface modification with hydrophilic COOH–PEG–COOH (MW 600, Figure 1 D) was performed by ligand exchange in dichloromethane (DCM) under 1 h sonication. The resulting PEGylated RLNPs displayed colloidal stability in water (Figure 1 E) allowing them to be used under physiological conditions.

The RLNPs were visualized by transmission electron microscopy (TEM). **Figure 2**A displays the size and cubic morphology of the nanocrystals. Although clustering of the RLNP was observed on the TEM grid as a drying artifact, discrete particles were readily visible due to the high image contrast from the barium (high-Z value) component. Particle-

size analysis of the TEM micrograph shows a narrow distribution of RLNP with a mean of ≈14 nm (Figure 2 B). Crystal structure and composition of the RLNP were evaluated by powder X-ray diffraction (XRD) identifying the host as cubic $Ba_{0.55} Y_{0.3} F_2$ (ICDD Powder Diffraction File #04-005-9812, Supporting Information, Figure S1). In comparison to co-doped barium yttrium fluoride nanophosphors produced by the same process, these host crystals differ in morphology (cubic versus tetragonal) and stoichiometry ($Ba_{0.55} Y_{0.3} F_2$ versus $BaYF_5$) due to the nature and concentration of the dopants, a phenomenon described recently in the literature. [14]

Quantitative analysis of the RLNP atom ratios obtained by X-ray photoelectron spectroscopy (XPS) corresponds well to the host composition determined by XRD with proportions of Ba, Y, and F in a survey scan equivalent to $Ba_{0.55} Y_{0.3} F_2$ (Supporting Information, Figure S2A). Successful surface modification with PEG was also confirmed in high-resolution C1s XPS spectra from oleic acid and PEG-coated RLNP shown by a change of shape and shift of the C1s peak (Supporting Information, Figure S2B and S2C). In addition to enabling dispersion in aqueous solutions, the amphiphilic PEG was chosen for its ability to improve the serum half-life and overall in vivo bio-compatibility of the nanophosphor. Free terminal –COOH groups on end-grafted bifunctional PEG chains also provide functionality for conjugation of targeting agents, such as mAbs or peptides, to the RLNPs.

To characterize the optical properties of the RLNPs, their emission spectrum was collected with a CCD coupled spectrograph while the sample was irradiated with X-rays (50 kVp, Figure 2C). Here the barium component of the RLNPs serves as an effective X-ray absorber with a K-edge at 37.4 keV, which lies within the diagnostic X-ray range. Energy transfer from the host lattice to luminescent centers was observed in characteristic Eu^{3+} emission peaks at 597 and 615 nm due to the $^5D_0 \rightarrow ^7F$ (magnetic-dipole) and $^5D_0 \rightarrow ^7F_{12}$ (electronic-dipole) transitions, respectively. In addition, a significant peak at 692 nm resulting from $^5D_0 \rightarrow ^7F_4$ transitions within the so-called "biological window" was also observed. In this NIR spectral region, hemoglobin and water/lipids have their lowest absorption coefficient allowing for imaging deeper in tissue. [15,16] The emission peaks of the RLNPs result from the electron configuration of the Eu^{3+} dopant, which serve as trap states within the band gap. [17] In lanthanide dopants, optical transitions within the 4f orbitals are shielded from interaction with the chemical environment by the 5s and 5p shells, which are lower in energy but spatially located outside of the 4f orbitals. [15] This unique photophysical feature enables RLNP emission tuning and potentially multiplex imaging by varying dopants in the nanophosphor.

Luminescence of the RLNP excited by β^+-decay of ^{18}F, commonly employed in PET tracers such as fluorodeoxyglucose (FDG), was examined using a conventional small-animal optical imaging system (IVIS Spectrum, Caliper, Hopkinton, MA). Solutions containing various concentrations of RLNPs (0, 0.1, 1.0, 5.0, and 10 mg mL^{-1}) and a range of FDG activity (3.0, 16, and 33 μ μCi at the start of the measurements) were imaged with 700 nm and open emission (490–850 nm) filters (Supporting Information, Figure S3). In addition, the characteristic Eu^{3+} emission spectrum of the RLNPs stimulated by FDG was verified through serial imaging with 500–800 nm emission filters (Supporting Information, Figure

S4). A plot of the RLNP optical emission at 700 nm illustrates a near-linear increase in luminescence with radioactivity for all samples measured (**Figure 3** A). RLNP samples containing ≥ 1 mg mL^{-1} displayed luminescence intensity above that of the FDG control. Light emitted purely from FDG is attributed to Cerenkov radiation, a phenomenon in which a charged particle passes through a dielectric medium at a speed greater than the speed of light in that medium resulting in the emission of light. [18,19] Although an optical signal from the lowest concentration sample (0.1 mg mL^{-1}) was not significantly detectable above the Cerenkov radiation background (a continuous spectrum with peak emission in the UV), further investigation of optimal dopant concentrations and modification of the RLNP to prevent surface quenching of luminescent centers (i.e., formation of a core–shell structure) is likely to vastly improve radioluminescence efficiency. Rapidly growing interest in Cerenkov-based optical imaging using PET tracers has recently inspired the use of QDs to red-shift Cerenkov luminescence toward tissue penetrating NIR. [20–24] Here RLNP may function in a similar manner and benefit from both direct UV excitation of the Eu^{3+} luminescent center and scintillation from the cascade of energetic electrons induced by positron interactions within the host. To briefly investigate the optical properties of the RLNP, radioluminescence measurements acquired with FDG and under open filter conditions were analyzed (Figure 3 B). Interestingly, samples containing lower concentrations RLNP (0.1 and 1.0 mg mL^{-1}) with 33 μCi FDG displayed decreased total light output compared to the FDG control suggesting that the UV-emission by Cerenkov radiation was attenuated by various absorption and energy transfer phenomena. However, samples containing the highest concentration of RLNP (10 mg mL^{-1}) displayed increased radioluminescence intensities suggesting stimulation of photons by higher-energy particles or photons in addition to potential UV excitation. These results suggest that further investigation of the photo-physical mechanisms of these nanomaterials is warranted.

To demonstrate the application of RLNPs under biological conditions, pseudo tumors where formed by subcutaneous injection of matrigel containing FDG (left) or FDG w/RLNPs (right). PET imaging was performed to visualize the presence of FDG in the inclusions (**Figure 4**A). Equal quantities of the radioisotope (≈ 55 μCi) in each pseudo tumor were verified by summing the total activity over each inclusion in the PET image and by comparing the optical signal in the Cerenkov luminescence image (Supporting Information, Figure S5). FDG-stimulated optical imaging of the mice bearing inclusions clearly displayed enhanced emission at 700 nm on the flank containing RLNPs (Figure 4 B). A low-intensity signal was also detected from the FDG inclusion due to the Cerenkov luminescence. To evaluate X-ray radioluminescence of the biological samples, the mice were sacrificed and frozen for > 1 week to allow for complete decay of the ^{18}F (half-life 2 hours) and warmed to 37 ° C prior to imaging in a custom X-ray optical imaging system, described previously. [6] Luminescence generated by RLNPs was observed from the corresponding inclusion upon X-ray excitation (Figure 4 C). No detectable signal was observed in the decayed FDG inclusion. The preceding results demonstrate the feasibility of applying RLNPs to enable radioluminescence detetection in these novel imaging modalities.

In summary, we have presented a facile synthesis and surface modification process to produce water-soluble radioluminescent cubic $Ba_{0.55}Y_{0.3}F_2:Eu^{3+}$ nanophosphors.

Physiochemical and luminescence characterization of the RLNPs confirm their structure, size, morphology, and optical properties critical to their ability to function as radioluminescent bioimaging probes. Although bulk phosphors and scintillators have been well studied for various technological applications, the unique properties of colloidal nanophosphors warrant further investigation into their photophysical mechanisms. As bioimaging probes, RLNPs offer several advantages over pure optical-based imaging agents, including greater tissue penetration, elimination of autofluoresence, simplified tomographic image reconstruction, and inherent multimodality with conventional radiological imaging techniques. Disadvantages of in vivo RLNP imaging are the use of ionizing radiation and the unknown long-term toxicity and clearance of these nanomaterials, although such limitations do not preclude their near-term use as tools in preclinical small animal imaging studies. As proof-of-principle demonstration, PEGylated RLNPs under biological conditions were shown to emit luminescence under excitation by either ^{18}F radioisotope or X-rays. This capability provides the potential to enable novel imaging modalities, such as XLCT or deep tissue Cerenkov luminescence imaging.

Experimental Section

Materials

Barium acetylacetonate hydrate, oleic acid, 1-octadecene, poly(ethylene glycol) diacid (MW 600), and dichloromethane (DCM) were purchased from Sigma–Aldrich (St. Louis, MO). Trifluoroacetic acid (CF_3COOH) and 200 proof ethanol (EtOH) were purchased from Fisher Chemical (Fairlawn, NJ). Europium oxide (Eu_2O_3), yttrium oxide (Y_2O_3) and toluene were purchased from Acros Organics (Morris Plains, NJ). All reagents were used without further purification. Deionized (D.I.) water was obtained from an ultrapure water purification system (Barnstead Nanopure, Thermo Scientific, Dubuque, IA). Matrigel was purchased from BD Biosciences (San Diego, CA).

Nanophosphor Synthesis

Eu^{3+}-doped barium yttrium fluoride radioluminescent nanophosphors (RLNPs) were synthesized by a thermodegradation of organometallic precursors in the presence of oleic acid and 1-octadecene. [11 –13] Briefly, europium and yttrium trifluoroacetates were obtained through dissolution of corresponding oxides (16.2 mg Eu_2O_3 and 208 mg Y_2O_3) in trifluoroacetic acid over 48 h at 27 °C. [25] The resulting trifluoroacetate products were isolated by distillation and combined with barium acetylacetonate (1.0 g). The mixture of organometallic precursors was then dissolved in octadecene/ oleic acid (40 mL, 1:1 v/v). The solution was sonicated for 15 min to ensure dissolution of the solid reagents and facilitate degassing of the solvent. The homogenized solution was then heated to 120 °C and stirred under vacuum for 15 min, heated further to 300 °C under argon atmosphere for 1 h, and subsequently allowed to cool to room temperature. The resulting colloidal mixture was combined with EtOH (200 mL) to precipitate the oleic acid-capped RLNPs. The flocculated RLNPs were isolated by decanting the solvent and further purified by redispersing the nanophosphors in toluene (10 mL) followed by precipitation and decanting with EtOH for two additional cycles of washing. The isolated oleic acid coated RLNPs were then dispersed in DCM (200 mL) for surface modification with diacid PEG (2 mL) under ultrasonic

agitation (Branson Ultrasonic Corp., Danbury, CA) at 40 °C for 1 h. The resulting PEGylated RLNPs were isolated by evaporating the DCM and purified by three rounds of dispersion/centrifugation with D.I. water.

Nanophosphor Characterization

Transmission electron microscopy (TEM) samples were prepared by dipping 400 mesh copper grids (Veco, Ted Pella, Redding, CA) in a diluted suspension of RLNPs in toluene. The grids were then dried and imaged on a JEOL TEM1230 (Tokyo, Japan) operating at 80 KV. TEM images were acquired with a Gatan 967 (Pleasanton, CA) slow scan, cooled CCD camera. NIH ImageJ with the particle size analyzer (PSA) macro was used to calculate the particle size distribution. Powder X-ray diffraction (XRD) patterns were acquired from dried samples placed on a silicon holder with a PANalytical X'Pert (Almelo, Netherlands) diffractometer using Cu-Kα radiation ($\gamma = 1.541$ Å) at 40 kV and 20 mA. X-ray photoelectron spectroscopy (XPS) analysis were carried out using a Surface Science Instrument S-probe spectrophotometer (Newburyport, MA) with a monochromatized Al X-ray source and 5 eV flood gun for charge neutralization. XPS samples were prepared by drying a film of RLNPs on an aluminum sheet. X-ray spot size for the acquisition was approximately 800 μm. Pressure in the analytical chamber during spectral acquisition was less than 5×10^{-9} Torr.

X-ray Radioluminescence Characterization and Imaging

To acquire the radioluminescence emission spectrum of the RLNP, a pelletized sample irradiated with X-ray source (50 kVp, Nucletron, Oldelft, Netherlands) was collected with a CCD coupled spectrograph (Princeton Instruments, Trenton NJ). X-ray radioluminescence imaging was performed on biological samples at 37 °C using a custom system described previously. [6]

FDG Radioluminescence Characterization and Imaging

Luminescence stimulated by positron emission was examined by mixing various concentrations of RLNPs with FDG in wells of a 96-well plate. The samples containing the described quantities of RLNPs (0, 0.1, 1.0, 5.0, and 10 mg mL^{-1}) and FDG (3.0, 16, and 33 μCi at the start of the measurements) were 200 μL in volume. Imaging was performed using a conventional small-animal optical imaging system (IVIS Spectrum, Caliper, Hopkinton, MA). Image analysis was conducted using MATLAB. Optical filter transmission, radioactive decay, and flat-field corrections were applied to the images. Photon count (average and standard deviation) was measured within circular regions-of-interests centered on each well.

In Vivo Radioluminescence Imaging

All animal studies were performed in accordance to IACUC guidelines. Nude mice ($n = 3$) were subcutaneously injected with a mixture of matrigel and FDG (left flank) and a mixture of matrigel, FDG, and 20 mg RLNP (right flank). MicroPET imaging of the mice was performed on a small-animal PET R4 rodent model scanner (Siemens Medical Solutions

USA, Inc., Knoxville, TN). Optical imaging of FDG-stimulated radioluminescence was performed using a conventional small-animal optical imaging system (IVIS Spectrum).

Supplementary Material

Refer to Web version on PubMed Central for supplementary material.

Acknowledgments

References

1. Shen J, Sun LD, Yan CH. Dalton Trans. 2008; 42:5687. [PubMed: 18941653]

2. Wang F, Banerjee D, Liu Y, Chen X, Liu X. Analyst. 2010; 135:1839. [PubMed: 20485777]

3. Nyk M, Kumar R, Ohulchanskyy TY, Bergey EJ, Prasad PN. Nano Lett. 2008; 8:3834. [PubMed: 18928324]

4. Chen G, Ohulchanskyy TY, Kumar R, Agren H, Prasad PN. ACS Nano. 2010; 4:3163. [PubMed: 20509664]

5. Zhou J, Sun Y, Du X, Xiong L, Hu H, Li F. Biomaterials. 2010; 31:3287. [PubMed: 20132982]

6. Carpenter CM, Sun C, Pratx G, Rao R, Xing L. Med. Phys. 2010; 37:4011. [PubMed: 20879562]

7. Pratx G, Carpenter CM, Sun C, Rao RP, Xing L. Opt. Lett. 2010; 35:3345. [PubMed: 20967061]

8. Pratx G, Carpenter CM, Sun C, Xing L. IEEE Trans. Med. Imaging. 2010; 29:1992. [PubMed: 20615807]

9. Byrne JD, Betancourt T, Brannon-Peppas L. Adv. Drug. Deliv. Rev. 2008; 60:1615. [PubMed: 18840489]

10. Sun C, Lee JS, Zhang M. Adv. Drug. Deliv. Rev. 2008; 60:1252. [PubMed: 18558452]

11. Vetrone F, Mahalingam V, Capobianco JA. Chem. Mater. 2009; 21:1847.

12. Boyer JC, Vetrone F, Cuccia LA, Capobianco JA. J. Am. Chem. Soc. 2006; 128:7444. [PubMed: 16756290]

13. Zhang YW, Sun X, Si R, You LP, Yan CH. J. Am. Chem. Soc. 2005; 127:3260. [PubMed: 15755126]

14. Wang F, Han Y, Lim CS, Lu Y, Wang J, Xu J, Chen H, Zhang C, Hong M, Liu X. Nature. 2010; 463:1061. [PubMed: 20182508]

15. Ntziachristos V, Bremer C, Weissleder R. Eur. Radiol. 2003; 13:195. [PubMed: 12541130]

16. Weissleder R. Nat. Biotechnol. 2001; 19:316. [PubMed: 11283581]

17. Werts MHV. Sci. Prog. 2005; 88:101. [PubMed: 16749431]

18. Cerenkov PA. Phys. Rev. 1937; 52:0378.

19. Ross HH. Anal. Chem. 1969; 41:1260.

20. Robertson R, Germanos MS, Li C, Mitchell GS, Cherry SR, Silva MD. Phys. Med. Biol. 2009; 54:N355. [PubMed: 19636082]

21. Spinelli AE, D'Ambrosio D, Calderan L, Marengo M, Sbarbati A, Boschi F. Phys. Med. Biol. 2010; 55:483. [PubMed: 20023328]

22. Liu H, Ren G, Miao Z, Zhang X, Tang X, Han P, Gambhir SS, Cheng Z. PLoS One. 2010; 5:e9470. [PubMed: 20208993]

23. Liu H, Zhang X, Xing B, Han P, Gambhir SS, Cheng Z. Small. 2010; 6:1087. [PubMed: 20473988]

24. Dothager RS, Goiffon RJ, Jackson E, Harpstrite S, Piwnica-Worms D. PLoS One. 2010; 5:e13300. [PubMed: 20949021]

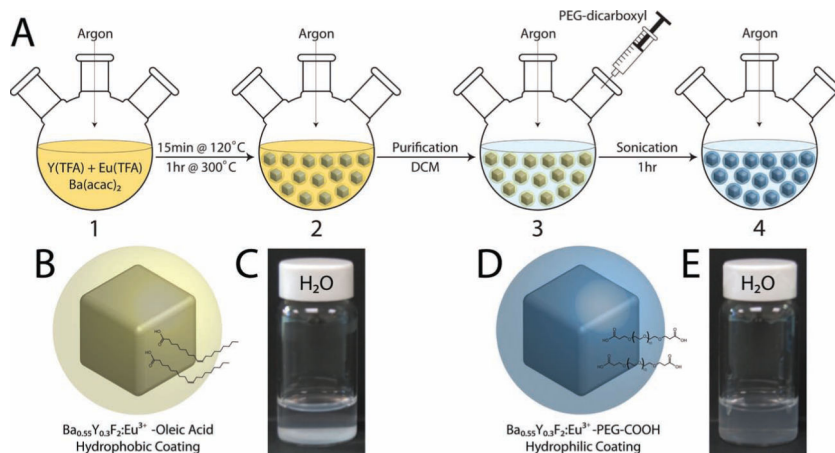25. Russel C. J. Non-Cryst. Solids. 1993; 152:161.

Figure 1.
Illustration of the PEGylated RLNP synthesis process and resulting products in deionized water. A) Stepwise nanophosphor synthesis and surface modifi cation procedure. B) Product of thermal degradation reaction, steps 1–2, and C) flocculated oleic acid capped RLNP dispersed in H_2O (10 mg mL^{-1}). D) COOH–PEG–COOH-coated RLNP produced through ligand exchange. E) Aqueous dispersion of hydrophilic RLNP (10 mg mL^{-1}).
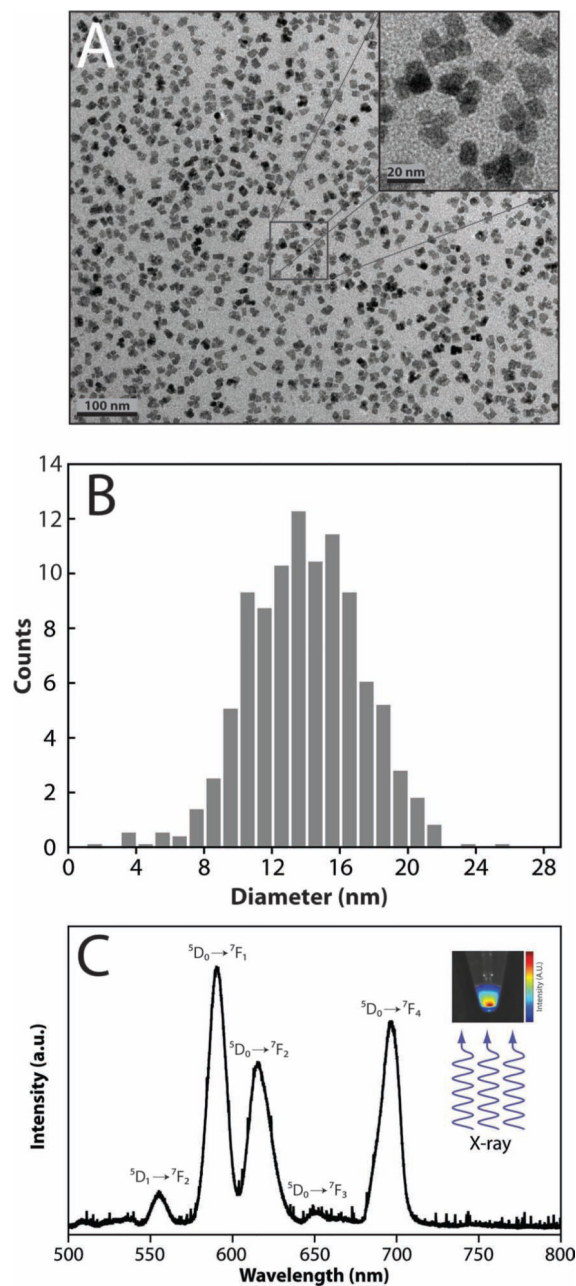
Figure 2.
Nanophosphor size and radioluminescence characterization. A) TEM of PEGylated barium yttrium fluoride RLNP displaying uniform cubic morphology. B) Size distribution of RLNP calculated by analysis of (A) displaying a mean size of ~ 14 nm. C) X-ray luminescence spectrum displaying characteristic Eu^{3+} peaks at 597, 615, and 692 nm. Inset: photograph of luminescence observed from a pelletized sample.
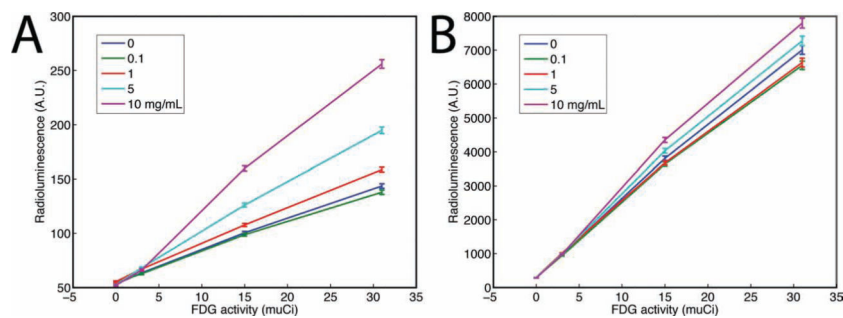
Figure 3.
Radioluminescence measurements acquired from RLNPs as a function of FDG activity. A) RLNP emission at 700 nm. B) Radioluminescence collected under open fi lter (490– 850 nm). Error bars represent pixel-to-pixel variation within a region of interest and propagated over three samples.
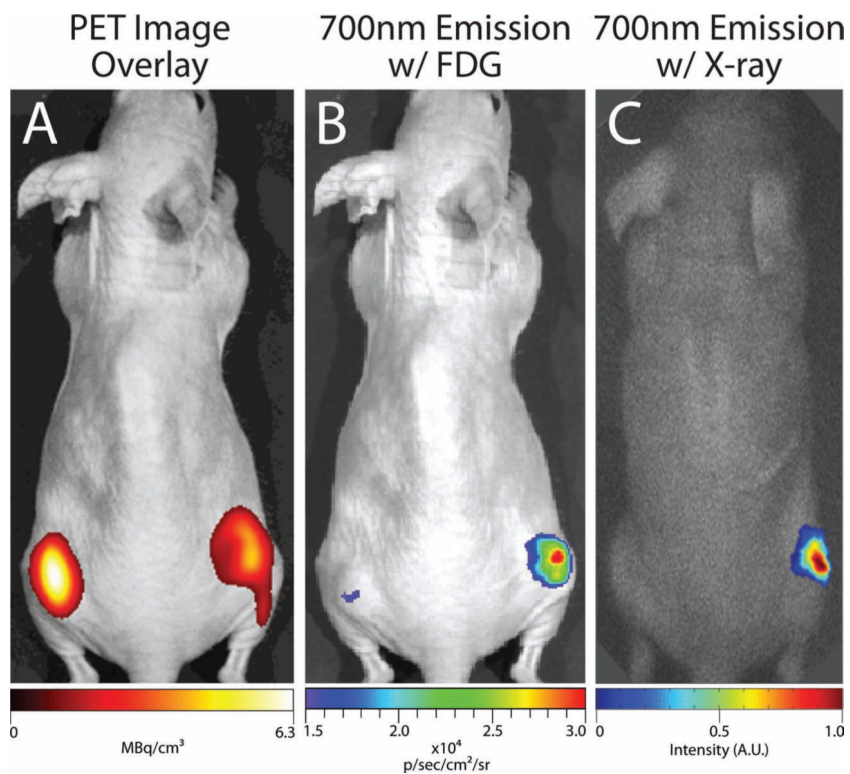
Figure 4.
Representative images of nude mouse bearing matrigel inclusions: matrigel w/FDG only (left) and matrigel w/20 mg RLNP + FDG (right). A) PET image. B) FDG-stimulated 700 nm radioluminescence emission image. C) X-ray radioluminescence image obtained after decay of FDG.